JACS
JOURNAL OF THE AMERICAN CHEMICAL SOCIETY
Article
Cite This: J. Am. Chem. Soc. 2019, 141, 1742−1748
pubs.acs.org/JACS

Strong Phonon−Phonon Interactions Securing Extraordinary Thermoelectric $Ge_{1-x}Sb_xTe$ with Zn-Alloying-Induced Band Alignment

Min Hong,[†,‡] Yuan Wang,[†] Tianli Feng,[§,∥] Qiang Sun,[‡] Shengduo Xu,[‡] Syo Matsumura,[⊥] Sokrates T. Pantelides,[§,∥] Jin Zou,*[,‡,#] and Zhi-Gang Chen*[,†,‡]

[†]Centre for Future Materials, University of Southern Queensland, Springfield, Queensland 4300, Australia
[‡]Materials Engineering, The University of Queensland, Brisbane, Queensland 4072, Australia
[§]Department of Physics and Astronomy and Department of Electrical Engineering and Computer Science, Vanderbilt University, Nashville, Tennessee 37235, United States
[∥]Materials Science and Technology Division, Oak Ridge National Laboratory, Oak Ridge, Tennessee 37831, United States
[⊥]Department of Applied Quantum Physics and Nuclear Engineering, Kyushu University, Motooka 744, Nishi-ku, Fukuoka 819-0395, Japan
[#]Centre for Microscopy and Microanalysis, The University of Queensland, Brisbane, Queensland 4072, Australia

Supporting Information

ABSTRACT: The ability of substitution atoms to decrease thermal conductivity is usually ascribed to the enhanced phonon-impurity scattering by assuming the original phonon dispersion relations. In this study, we find that 10% Sb_{Ge} alloying in GeTe modifies the phonon dispersions significantly, closes the acoustic−optical phonon band gap, increases the phonon−phonon scattering rates, and reduces the phonon group velocities. These changes, together with grain boundaries, nanoprecipitates, and planar vacancies, lead to a significant decrease in the lattice thermal conductivity. In addition, an extra 2−6% Zn alloying decreases the energy offset between valence band edges at L and Σ points in $Ge_{1-x}Sb_xTe$ that is found to be induced by the Ge $4s^2$ lone pairs. Since Zn is free of s^2 lone pair electrons, substituting Ge with Zn atoms can consequently diminish the Ge $4s^2$ lone-pair characters and reduce the energy offset, resulting in two energetically merged valence band maxima. The refined band structures render a power factor up to 40 μW cm^{-1} K^{-2} in $Ge_{0.86}Sb_{0.1}Zn_{0.04}Te$. Ultimately, a superhigh zT of 2.2 is achieved. This study clarifies the impacts of high-concentration substitutional atoms on phonon band structure, phonon−phonon scattering rates, and the convergence of electron valence band edges, which could provide guidelines for developing high-performance thermoelectric materials.

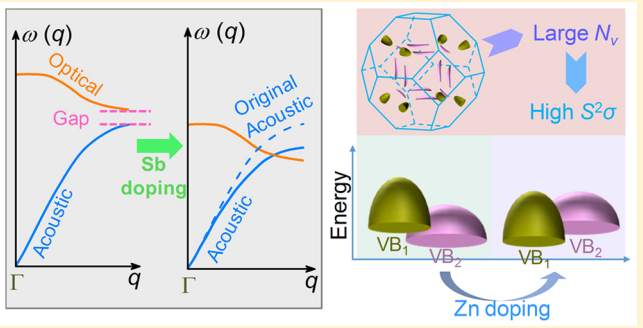

INTRODUCTION

Thermoelectrics, featured by the capability of interconversion between heat and electricity, have become a typical component in the drive for eco-friendly energy technology.[1] The mass-market commercialization of thermoelectric devices demands a sufficiently high energy conversion efficiency, which depends upon the thermoelectric properties of electrical conductivity (σ), Seebeck coefficient (S), and thermal conductivity (κ, comprising electronic κ_e and lattice κ_l contributions).[2,3] To turn these into a single parameter to gauge the thermoelectric efficiency at a given operating temperature (T), the figure-of-merit (zT) is formulated as $zT = S^2\sigma T/\kappa$.[4] The enhancement of thermoelectric performance generally involves κ_l minimization and power factor ($S^2\sigma$) enhancement, which depend on the transport of phonons and free charge carriers, respectively.[5]

The two common strategies for decreasing κ_l are to strengthen the inherent phonon−phonon interactions and to introduce extra phonon-scattering sources.[6] The former suggests to seek/amend materials comprising heavy elements, a complex unit cell with high symmetry, weak chemical bonds, and strong lattice anharmonicity.[5,7] Materials such as SnSe,[8−10] Ag_8SnSe_6,[11] $K_2Bi_8Se_{13}$,[12] and $AgSbTe_{2-x}Se_x$[13] with the mentioned descriptor(s) show low κ_l and thus outstanding zT. The extra phonon-scattering sources, for instance, grain boundaries,[14−17] precipitates,[18−22] impurities,[23,24] and various types of lattice imperfections,[25−29] focus on minimizing the phonon relaxation time. Among the lattice imperfections, the decreased κ_l caused by point defects is intuitively ascribed to phonon

Received: November 25, 2018
Published: December 28, 2018

DOI: 10.1021/jacs.8b12624
J. Am. Chem. Soc. 2019, 141, 1742−1748

scattering by mass fluctuations and lattice distortions. By definition, a phonon is the quantized energy of lattice vibrations, which can be simplified as a spring and mass system.[30] Large concentrations of substitutional atoms change the host mass and, in turn, may affect the inherent phonon−phonon interactions. Thus, it is necessary to revisit the impact on phonon scattering.

Band engineering has been proven to bypass the $S^2\sigma$ peak corresponding to the optimal carrier concentration.[31,32] In rock-salt chalcogenides, the two valence bands at L (VB_L) and Σ (VB_Σ) points provide additional room to enhance $S^2\sigma$ via minimizing the energy offset between the two-valence-band maxima.[33−35] Conventional band engineering is based on the experimental approach to test the appropriate substitutions. Understanding the chemical nature of VB_L and VB_Σ can help efficiently screen optimal substitutions from a theoretical perspective.

GeTe is a promising midtemperature *p*-type thermoelectric material.[36,37] To suppress the intrinsically high hole concentration stemming from the Ge vacancies, GeTe is commonly alloyed with aliovalent elements (for example, Sb[38] and Bi[39]). Examination of phonon transport in these alloys can disclose the effect of point defects on inherent phonon−phonon interactions. Moreover, GeTe has a rhombohedral-to-cubic phase transition at ∼700 K and has the degenerate evolution of multiple valence band edges.[40] Understanding the band structures of GeTe can reveal the chemical nature of these multiple valence bands.

Herein, we systematically investigate the effects of Sb and additional Zn alloying on thermoelectric properties of GeTe and the associated fundamentals. Besides tuning carrier concentration, Sb alloying results in the crossover of acoustic and optical phonon branches and flattens the acoustic phonon dispersion to decrease the phonon group velocity (v) of GeTe, as schematically shown in Figure 1a. Together with the extra scattering sources including grain boundaries, precipitates, planar vacancies, and point defects (Figure 1b), phonon scattering is greatly enhanced. Consequently, the obtained κ_l of $Ge_{0.9}Sb_{0.1}Te$ alloys is reduced by 55% at 300 K with respect to that of GeTe; refer to Figure 1c. Electronically, our theoretical analysis indicates that, in both rhombohedral (R-) and cubic (C-) GeTe, the two valence band edges at L and Σ points are attributed to the slightly more Ge $4s^2$ lone pair character (as indicated by the red spots in Figure 1d) in the highest occupied molecular orbital (HOMO). Therefore, high-level substituted elements free of the s^2 lone pair orbital (for example, Zn) can diminish the energy offset between these two valence band edges via partially reducing the cation s^2 lone pair character on HOMO. Thus, Zn-alloyed $Ge_{0.9}Sb_{0.1}Te$ has larger band degeneracy (N_v), leading to an enhanced $S^2\sigma$ (Figure 1e). Overall, as shown in Figure 1f, the significantly decreased κ_l and enhanced $S^2\sigma$ lead to a superhigh peak zT ranging from 2.0 to 2.5 with an average value of 2.2 in our $Ge_{0.86}Sb_{0.1}Zn_{0.04}Te$ (10% Sb and 4% Zn) during three heating−cooling cycle measurements (Figure S1).

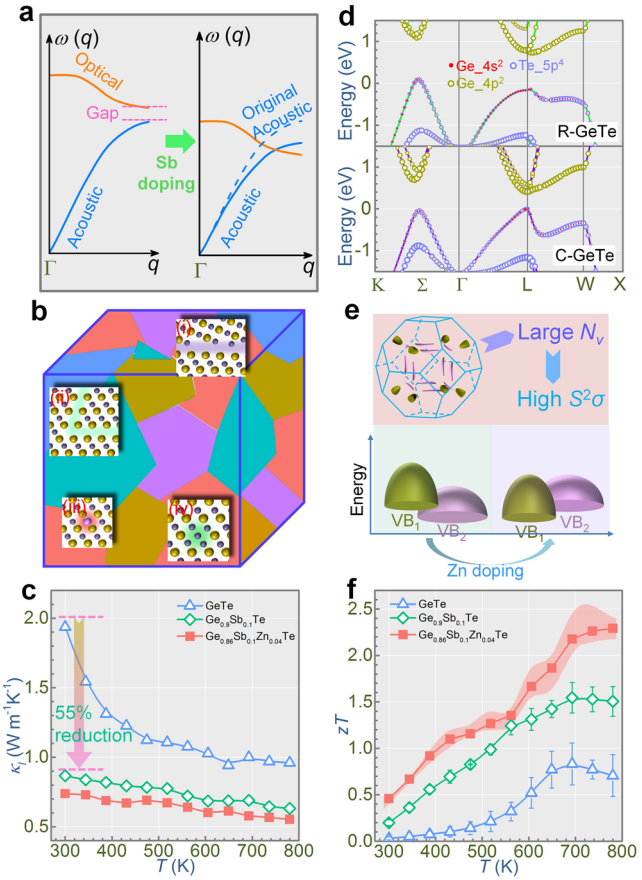

Figure 1. Methodology for performance enhancement in GeTe-based thermoelectric materials. (a) Schematic diagram demonstrating the evolution of phonon dispersions due to Sb substitution on Ge sites. (b) Schematic diagram showing the sintered polycrystalline bulk composed of grain boundaries (i), planar vacancies (ii), point defects (iii), and precipitates (iv). (c) Temperature-dependent lattice thermal conductivity (κ_l) for the representative GeTe, $Ge_{0.9}Sb_{0.1}Te$, and $Ge_{0.86}Sb_{0.1}Zn_{0.04}Te$. (d) Band structures for GeTe with the orbital characters indicated by the symbol sizes. The up and bottom panels correspond to rhombohedral and cubic GeTe, respectively. (e) Convergence of multiple valence band edges due to Zn alloying. (f) Measured temperature-dependent figure-of-merit (zT) with the red background color showing the zT range measured during three heating−cooling cycles.

RESULTS AND DISCUSSION

Phonon Dispersion Relations. To evaluate the thermoelectric performance, the as-obtained Zn-doped $Ge_{1-x}Sb_xTe$ powders without appreciable impurities (refer to X-ray diffraction (XRD) patterns in Figures S2 and S3) were compressed into pellets using spark plasma sintering (SPS). The measured temperature-dependent thermoelectric properties are summarized in Figures S4 and S5. As can be seen, one of the key reasons for the extraordinary high zT is the remarkably decreased κ_l. To elucidate the fundamentals related to the lattice dynamics, we performed density functional theory (DFT) calculations. Figure 2a exhibits the calculated phonon dispersion of R-GeTe. The three lowest dispersions at the Γ point are indexed as the in-plane transverse acoustic mode (TA), the in-plane longitudinal acoustic mode (LA), and the out-of-plane flexural acoustic mode (ZA).[41] The optical phonon branches occupy quite high eigenvalues, yielding the separation of acoustic and optical phonon modes in the pristine GeTe. Such an acoustic-optical frequency gap (a−o gap) is clearly identified in the calculated phonon density of states (DOS) (refer to the right panel of Figure 2a) near 3 THz. The isolation of acoustic modes from optical modes leads to less phonon−phonon scattering channels in pristine GeTe, namely weak inherent phonon scattering. The comparison of phonon DOS and projected DOS (PDOS) illustrates that Ge

DOI: 10.1021/jacs.8b12624
J. Am. Chem. Soc. 2019, 141, 1742−1748

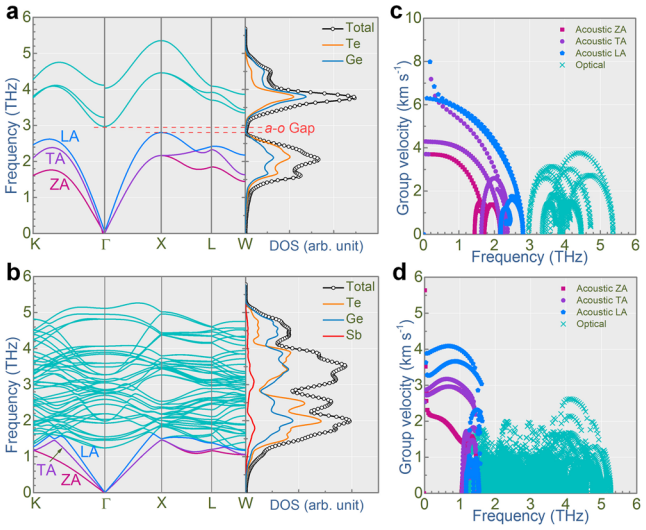

Figure 2. Calculated phonon dispersions and phonon DOS. (a) Rhombohedral (R-) GeTe and (b) Sb-doped R-GeTe. Calculated phonon group velocity (v) for (c) R-GeTe and (d) Sb-doped R-GeTe.

and Te dominate the optical modes and acoustic modes, respectively. This observation agrees with the reported theoretical study of phonon dynamics, which revealed that the acoustic (optical) phonon branch is governed by the constituting atom with larger (smaller) mass.[42] Phonon DOS analysis together with the fact that the atomic mass of Ge is only one-third of that of Te rationalize the observed a–o gap in the pristine GeTe.[42] We calculated the phonon dispersions for C-GeTe, shown in Figure S6. There are imaginary optical modes at Γ for C-GeTe, suggesting some optical branches lower than acoustic branches. Therefore, the phonon dispersions of C-GeTe cannot provide information on phonon–phonon scattering strength based on frequency gap.

Figure 2b shows the calculated phonon dispersion of R-$Ge_{0.9}Sb_{0.1}Te$. Since the calculation of $Ge_{0.9}Sb_{0.1}Te$ is based on the supercell, there exist more optical branches than GeTe, which is based on a primitive cell. The Sb alloying induces dispersive optical phonon branches, resulting in the optical modes going beyond the acoustic modes. The crossover of optical modes and acoustic modes is anticipated to strengthen acoustic–optical interactions in $Ge_{0.9}Sb_{0.1}Te$. According to the calculated phonon DOS (right panel of Figure 2b), the high-frequency peak of PDOS contributed by Sb is close to the frequency region where the a–o gap exists in the pristine GeTe. Substituting Sb on the Ge sites shifts the optical modes down to lower frequency range, leading to the crossover of acoustic and optical phonon branches. By theory, the a–o gap of the pristine GeTe results from the large atomic mass difference between cation (Ge) and anion (Te).[30,42] Alloying with Sb increases the average cation mass and brings the mass ratio between cation and anion close to one, which further supports the crossover of acoustic and optical branches in $Ge_{0.9}Sb_{0.1}Te$. Since the substitution of light atoms on Te sites can also reduce the atomic mass ratio between cation and anion, we expect that it can enhance the phonon–phonon scattering as well.

The calculated scattering rates reveal that Sb alloying can indeed enhance the phonon–phonon interactions, especially in the low-frequency range (refer to Figure S8). Note that the calculations are based on the supercell, which assumes Sb atoms are distributed uniformly in the lattice. In the real cases, the random distribution can induce an extra disorder scattering, which might not be important compared to the significantly modified phonon band structure and the phonon–phonon scattering.

Moreover, the low-frequency dispersion (i.e., acoustic modes) is flattened, suggesting the reduction of v, which is given by the slope of the acoustic dispersion relation.[43] Parts c and d of Figure 2 manifest the determined v as a function of phonon frequency for GeTe and $Ge_{0.9}Sb_{0.1}Te$, respectively. As can be seen, alloying with Sb indeed decreases v, which is caused by the heavy atomic mass of Sb.[7]

Microstructure Characterizations. In addition to the enhanced phonon–phonon interactions caused by Sb alloying, microstructures can serve as extra phonon scattering sources to decrease κ_l. Figure 3a is a transmission electron microscope (TEM) image obtained from the sintered $Ge_{0.86}Sb_{0.1}Zn_{0.04}Te$ pellet. We can observe the microscale grains and high-density nanoprecipitates embedded in the matrix. The corresponding

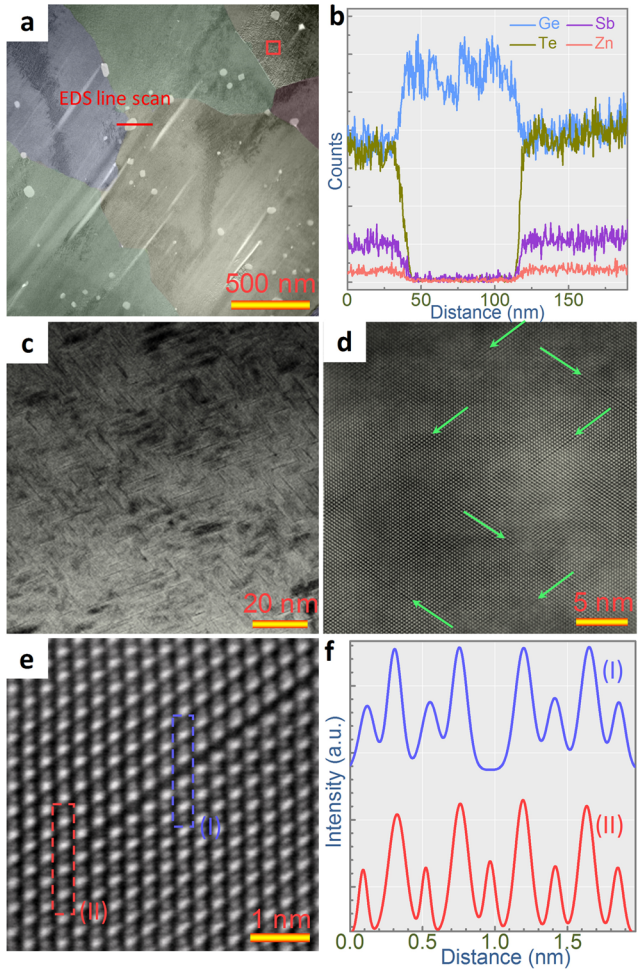

Figure 3. Microstructure characterizations of $Ge_{0.86}Sb_{0.1}Zn_{0.04}Te$. (a) Typical transmission electron microscope (TEM) image showing the multiple grains and nanoprecipitates. (b) Energy-dispersive X-ray spectroscopy (EDS) line scan studying the composition of precipitates. (c) Enlarged TEM image showing the network of stripes. (d) High-angle annular dark-field (HAADF) scanning TEM (STEM) image indicating planar vacancies. (e) Amplified HAADF STEM image of a representative planar vacancy. (f) Line profile along the framed atomic columns in (e).

DOI: 10.1021/jacs.8b12624
J. Am. Chem. Soc. 2019, 141, 1742–1748

high-angle annular dark-field (HAADF) scanning TEM (STEM) image presents the dark contrast of nanoprecipitates, indicating the lighter component elements in nanoprecipitates than in the matrix (Figure S9). Figure 3b is the X-ray energy-dispersive spectroscopy (EDS) line scan across the precipitate indicating that the precipitates are Ge-rich.

The amplified TEM image taken from the area with dark contrast in Figure 3a reveals the presence of a network of high-density linear stripes (Figure 3c). The dark contrast may be caused by the strains arising from the stripes. Furthermore, we applied aberration-corrected STEM to investigate the atomic arrangement of the observed linear stripes. Figure 3d shows a high-resolution HAADF-STEM image, in which a few planar vacancies (marked by the green arrows) are evidently observed. Since R-GeTe is a slightly distorted face-centered cubic phase,[44] the observed planar vacancies can be considered as {111} planes of the pseudocubic structure. It is noteworthy that the planar vacancies are embedded in the randomly oriented grains so that planar vacancies do not exhibit preferential orientation in the sintered pellet. Consequently, the planar vacancies will not result in anisotropic thermoelectric properties. Figure 3e is a zoom-in image of HAADF-STEM to demonstrate the configuration of atoms in such a representative planar vacancy. The contrast of HAADF-STEM directly relates to the atomic number,[45] so that bright atomic columns are Te, whereas the dim atomic columns correspond to Ge. Figure 3f plots the intensity profiles obtained from the two framed atomic columns shown in Figure 3e. Peaks with low and high intensities correspond to Ge and Te atoms, respectively. Thus, the planar vacancies originate from the missing Ge atoms in the {111} plane. The TEM specimen was from the pellet measured several times to test the thermal stability of thermoelectric performance. The durability of corresponding thermoelectric properties (refer to Figure S1) suggests that the observed microstructures are preserved after heating−cooling cycles.

From the above comprehensive analysis, we can conclude that the remarkably decreased κ_l is linked to (i) the reinforced phonon−phonon interactions and decreased v induced by Sb alloying and (ii) the presence of various phonon scattering sources including grain boundaries, nanoscale precipitates, planar vacancies, and inevitable point defects resulting from Ge sites replaced by Sb/Zn atoms.

Modeling Study of Electronic Transport Coefficients. To elucidate the electronic transport behavior and the corresponding $S^2\sigma$ enhancement, we calculate the plots of S and Hall carrier mobility (μ_H) as a function of n_H using the single Kane band (SKB) model.[46] The measured temperature-dependent μ_H generally follows a power law of $T^{-1.5}$, indicative of the free charge-carrier scatterings being governed by acoustic phonons (refer to Figure S10).

Figure 4a shows the calculated plots of n_H-dependent S compared with the measured S versus n_H data points at both 300 and 700 K. Because the plot of $S - n_H$ is determined by m_d^*, the variation of S versus n_H with different compositions can reflect the alteration of band structures. The hollow data points corresponding to $Ge_{1-x}Sb_xTe$ generally follow a similar trend with n_H varying in a wide range upon different Sb contents. Therefore, Sb alloying does not notably modify m_d^*. However, the solid data points of $Ge_{0.9-y}Sb_{0.1}Zn_yTe$ follow totally different plots of S against n_H. Upon raising the Zn alloying ratio, the corresponding $S - n_H$ plot exhibits an upward trend. We quantitatively determined m_d^* according to

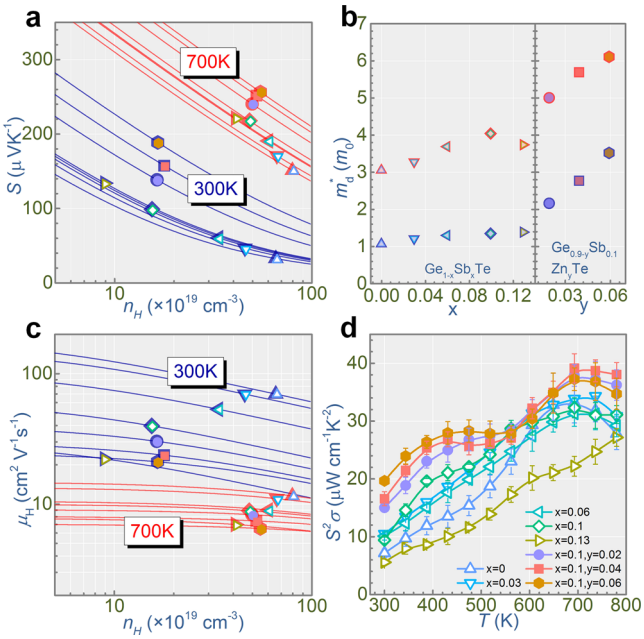

Figure 4. Examination of electronic transport coefficients using modeling simulations at 300 and 700 K. Calculated curves of Seebeck coefficient (S) (a) and Hall carrier mobility (μ_H) (c) as a function of Hall carrier mobility (n_H) compared with the measured data points versus n_H at 300 and 700 K. (b) Derived density-of-states effective mass (m_d^*) of $Ge_{1-x-y}Sb_xZn_yTe$. (d) Measured temperature-dependent power factor ($S^2\sigma$).

the measured S and n_H. Using the measured S, the reduced Fermi level (η) can be derived according to Equation S1. Then, substituting η into Equation S2, we can determine m_d^*. Figure 4b exhibits the determined m_d^* for different compositions at both 300 and 700 K. Zn alloying actually gives rise to m_d^*. Figure 4c shows the comparison of $\mu_H - n_H$ plots with the measured data points. As can be seen, μ_H decreases in $Ge_{1-x-y}Sb_xZn_yTe$ with increasing Sb and Zn substitution ratios, resulting from the increased charge-carrier scatterings.[47] The variations of m_d^* and charge-carrier scatterings will ultimately impact $S^2\sigma$. Figure 4d shows temperature-dependent $S^2\sigma$ for $Ge_{1-x-y}Sb_xZn_yTe$. Specifically, a maximal $S^2\sigma$ close to 40 μW cm^{-1} K^{-2} is achieved for the $Ge_{0.86}Sb_{0.1}Zn_{0.04}Te$ pellet. The enhanced $S^2\sigma$ can be ascribed to the optimized n_H by Sb and enlarged m_d^* by Zn.

Electronic Band Structures. To explore the evolution of band structures due to Sb alloying and the additional Zn alloying, we performed DFT calculations based on the 3 × 3 × 3 supercell of $Ge_{27}Te_{27}$. Parts a and b of Figure 5 display the band structures for both R- and C-$Ge_{27}Te_{27}$, respectively. The primary valence band edge shifts from Σ point to L point of the first Brillion zone during the R-to-C phase transition, agreeing with the reported band structure evolution of GeTe caused by the phase transition.[37] Parts c and d of Figure 5 present the band structures of $Ge_{24}Sb_3Te_{27}$ with R- and C-phases. Sb alloying does not notably change the band structures of both R- and C-GeTe. However, 4% Zn_{Ge} alloying can significantly modify the band structures, as shown in Figure 5e,f. The two valence band edges nearly locate at the same energy level after Zn alloying. In particular, Zn alloying realizes the exact convergence of VB_L and VB_Σ in the cubic $Ge_{24}Sb_3Te_{27}$.

Interestingly, Zn also produces an impurity band within the band gap (E_g) region close to the conduction band edge. The

DOI: 10.1021/jacs.8b12624
J. Am. Chem. Soc. 2019, 141, 1742−1748

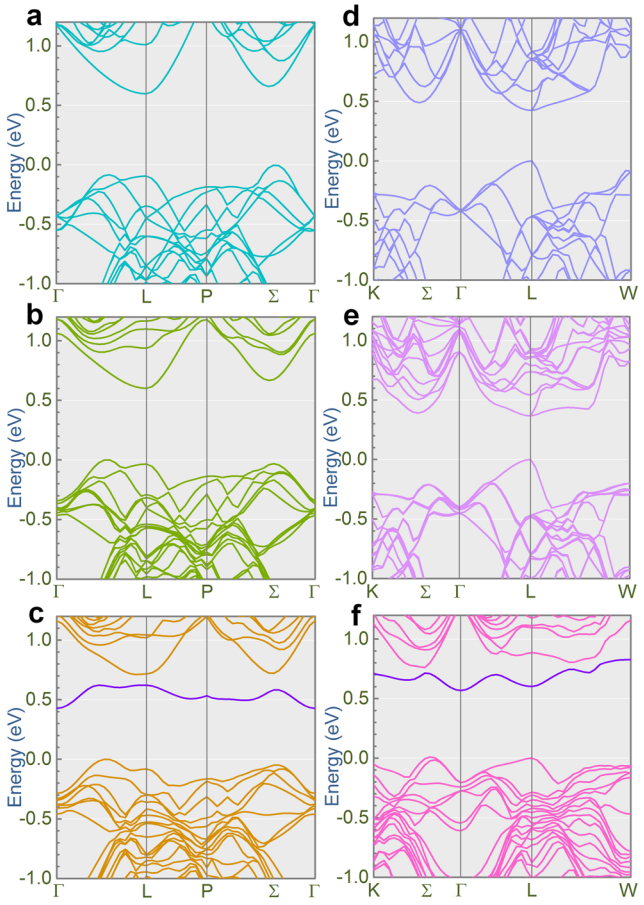

Figure 5. Examination of electronic band structures. (a) Rhombohedral (R-) $Ge_{27}Te_{27}$, (b) cubic (C-) $Ge_{27}Te_{27}$, (c) R-$Ge_{24}Sb_3Te_{27}$. (d) C-$Ge_{24}Sb_3Te_{27}$, (e) R-$Ge_{23}Sb_3ZnTe_{27}$, and (f) C-$Ge_{23}Sb_3ZnTe_{27}$.

energy separation between the impurity band and the VB is even larger than the E_g without Zn substitutions; therefore, the impurity band does not affect the electronic transport of *p*-type GeTe-based materials. Moreover, the determined E_g of C-GeTe, C-$Ge_{24}Sb_3Te_{27}$, and C-$Ge_{23}Sb_3ZnTe_{27}$ are 0.36, 0.4, and 0.55 eV. As can be seen, even with the impurity band considered, E_g is still enlarged in C-$Ge_{23}Sb_3ZnTe_{27}$. Since the bipolar thermal conduction occurs at high temperatures, Zn-doping is favorable to suppress the bipolar conduction.

Using the method of DFT calculation and molecular orbital theory, we discover that the slightly more Ge $4s^2$ lone pair character in the valence band edge at L determines the energy separation between VB_L and VB_Σ. The related discussion can be found in section 7 of the Supporting Information. Zn is free of s^2 lone pair electrons when bonding with Te. Consequently, Zn_{Ge} alloying can partially remove the weight of cation s^2 lone pair electrons on HOMO, accounting for the convergence of VB_L and VB_Σ.

CONCLUSIONS

We achieve a maximal zT value of ~2.2 in $Ge_{1-x-y}Sb_xZn_yTe$, stemming from the significantly decreased κ_l and increased $S^2\sigma$. Based on the comparison between phonon dispersions of GeTe and $Ge_{1-x}Sb_xTe$ alloys, we find that Sb induces the crossover of acoustic and optical phonon branches and further flattens the acoustic phonon modes, leading to strong acoustic-optical phonon interactions and low phonon velocity. The strong phonon−phonon scattering and the extra scattering sources demonstrated by TEM characterization synergistically lead to a significantly decreased κ_l. Moreover, additional Zn alloying is found to energetically merge the multiple valence band edges, due to the partially removed Ge $4s^2$ lone-pair characters on the valence band edge, which accounts for the reduced energy offset between these multiple valence band edges. The well-aligned valence band edges at nearly the same energy level lead to an enhanced $S^2\sigma$ in Zn-alloyed $Ge_{1-x}Sb_xTe$ at high temperature. The demonstrated strategy of strengthening phonon−phonon interactions and the revealed chemical nature of multiple valence band edges to screen suitable elements for band engineering can pave a robust route to develop high-performance thermoelectric materials.

EXPERIMENTAL SECTION

Material Synthesis. Elemental Ge, Te, Sb, and Zn were purchased from Sigma-Aldrich. Under high vacuum, these precursors were sealed in quartz tubes to synthesize $Ge_{1-x-y}Sb_xZn_yTe$. After heating to 950 °C within 12 h, quartz tubes were held for 6 h at this setting temperature and then quenched in ice−water. To release the strain, samples were annealed at 650 °C for 72 h. The obtained ingots were grounded into fine powders by ball milling. The collected powders were compressed into pellets by SPS under vacuum with the sintering condition of pressure = 55 MPa, temperature = 550 °C, and holding time = 5 min. Densities of obtained pellets were estimated by the Archimedes' method and corroborated to be ~97% of the theoretical value of GeTe (refer to Table S1).

Characterization. The phase characterizations were examined by XRD (Bruker D8 Advance MKII). The microstructure characterizations were performed by TEM of Philips Tecnai F20 and STEM of JEOL Arm200.

Thermoelectric Property Measurement. A laser flash method (LFA 457, NETZSCH) was used to measure thermal diffusivity (D) (plotted in Figure S14). The obtained values were cross-checked by the hyper flash method (LFA 467, NETZSCH). Then, κ was derived via $\kappa = DC_pd$, with d and C_p denoting the density and the specific heat capacity, respectively. C_p was determined using the Dulong−Petit law, which has been widely used in GeTe systems.[38,39,48,49] σ and S were measured using the ZEM-3, ULVAC, and the SBA 458, NETZSCH. The Hall measurement was conducted according to the Van der Pauw method with a magnetic field up to ±1.5T.[50] Based on the directly measured Hall coefficient (R_H), n_H and μ_H were determined by $n_H = 1/(eR_H)$ and $\mu_H = \sigma R_H$, in which e is the electron charge.

DFT Calculations. Band structure calculations were performed using the plane-wave self-consistent field (PWSCF) code. All of these DFT calculations were implemented in the QUANTUM-ESPRESSO.[51] The local density approximation (LDA) was used to describe the exchange and correlation interactions.[52] The cutoff sets of the kinetic energy and the electronic density were 40 and 640 Ry, respectively. In the calculations, we considered the spin−orbit coupling. Band structure calculations were based on the 3 × 3 × 3 supercell. To study band structures with alloying/doping, three Ge sites were replaced by Sb, and one Ge site was substituted by Zn. Phonon calculation of $Ge_{1-x}Sb_xTe$ was based on a supercell of 2 × 2 × 2 with one Ge replaced by Sb. The relaxation criterion of modified crystal structures was the force $<10^{-5}$ eV Å^{-1} on each atom. Supercells with atomic displacements were constructed by the Phonopy code[53] with the respective size being 3 × 3 × 3 for GeTe and 2 × 2 × 2 for $Ge_xSb_{1-x}Te$. After feeding into QUANTUM-ESPRESSO, the forces were calculated. Finally, the Phonopy code was used to determine the set of forces and then the phonon dispersions. The phonon−phonon scattering rates were calculated using the ShengBTE package.[54]

ASSOCIATED CONTENT

Supporting Information

The Supporting Information is available free of charge on the ACS Publications website at DOI: 10.1021/jacs.8b12624.

DOI: 10.1021/jacs.8b12624
J. Am. Chem. Soc. 2019, 141, 1742−1748

Details of modeling study, the thermal stability of thermoelectric properties, XRD patterns, temperature-dependent thermoelectric properties, determination of lattice thermal conductivity, calculated phonon scattering rate, additional TEM images, Hall measurement data, chemical natures of band structures, the density of states, thermal diffusivities, and densities (PDF)

AUTHOR INFORMATION

Corresponding Authors

*zhigang.chen@usq.edu.au, zhigang.chen@uq.edu.au
*j.zou@uq.edu.au

ORCID

Min Hong: 0000-0002-6469-9194
Tianli Feng: 0000-0002-7284-5657
Jin Zou: 0000-0001-9435-8043
Zhi-Gang Chen: 0000-0002-9309-7993

Notes

The authors declare no competing financial interest.

ACKNOWLEDGMENTS

The authors acknowledge the financial support provided by the Australian Research Council. Z.-G.C. thanks the USQ Strategic research fund and USQ start-up grant. J.Z. thanks the KU's Progress 100 program to encourage the UQ−KU collaboration, as well as the Nanotechnology Platform Project for advanced nanostructure characterization. The Centre for Microscopy and Microanalysis and the Research Computing Centre at UQ are acknowledged for providing characterization facilities and the computation clusters, respectively. Work at Vanderbilt University was supported by the US Department of Energy grant DE-FG02-09ER46554.

REFERENCES

(1) Snyder, G. J.; Toberer, E. S. Complex Thermoelectric Materials. *Nat. Mater.* **2008**, *7*, 105−114.
(2) He, J.; Tritt, T. M. Advances in Thermoelectric Materials Research: Looking Back and Moving Forward. *Science* **2017**, *357*, 1369.
(3) Zhu, T.; Liu, Y.; Fu, C.; Heremans, J. P.; Snyder, J. G.; Zhao, X. Compromise and Synergy in High-Efficiency Thermoelectric Materials. *Adv. Mater.* **2017**, *29*, 1605884.
(4) Zhao, L.-D.; Dravid, V. P.; Kanatzidis, M. G. The Panoscopic Approach to High Performance Thermoelectrics. *Energy Environ. Sci.* **2014**, *7*, 251−268.
(5) Zhu, H.; Xiao, C.; Xie, Y. Design of High-Efficient Thermoelectric Materials: Tailoring Reciprocal-Space Properties by Real-Space Modification. *Adv. Mater.* **2018**, *30*, 1802000.
(6) Chen, Z.-G.; Shi, X.; Zhao, L.-D.; Zou, J. High-Performance SnSe Thermoelectric Materials: Progress and Future Challenge. *Prog. Mater. Sci.* **2018**, *97*, 283−346.
(7) Chen, Z.; Zhang, X.; Pei, Y. Manipulation of Phonon Transport in Thermoelectrics. *Adv. Mater.* **2018**, *30*, 1705617.
(8) Zhao, L.-D.; Tan, G.; Hao, S.; He, J.; Pei, Y.; Chi, H.; Wang, H.; Gong, S.; Xu, H.; Dravid, V. P.; Uher, C.; Snyder, G. J.; Wolverton, C.; Kanatzidis, M. G. Ultrahigh Power Factor and Thermoelectric Performance in Hole-Doped Single-Crystal SnSe. *Science* **2016**, *351*, 141−144.
(9) Zhao, L.-D.; Chang, C.; Tan, G.; Kanatzidis, M. G. SnSe: a Remarkable New Thermoelectric Material. *Energy Environ. Sci.* **2016**, *9*, 3044−3060.
(10) Tang, G.; Wei, W.; Zhang, J.; Li, Y.; Wang, X.; Xu, G.; Chang, C.; Wang, Z.; Du, Y.; Zhao, L.-D. Realizing High Figure of Merit in Phase-Separated Polycrystalline $Sn_{1-x}Pb_xSe$. *J. Am. Chem. Soc.* **2016**, *138*, 13647−13654.
(11) Li, W.; Lin, S.; Ge, B.; Yang, J.; Zhang, W.; Pei, Y. Low Sound Velocity Contributing to the High Thermoelectric Performance of Ag_8SnSe_6. *Adv. Sci.* **2016**, *3*, 1600196.
(12) Pei, Y.; Chang, C.; Wang, Z.; Yin, M.; Wu, M.; Tan, G.; Wu, H.; Chen, Y.; Zheng, L.; Gong, S.; Zhu, T.; Zhao, X.; Huang, L.; He, J.; Kanatzidis, M. G.; Zhao, L.-D. Multiple Converged Conduction Bands in $K_2Bi_8Se_{13}$A Promising Thermoelectric Material with Extremely Low Thermal Conductivity. *J. Am. Chem. Soc.* **2016**, *138*, 16364−16371.
(13) Hong, M.; Chen, Z.-G.; Yang, L.; Liao, Z.-M.; Zou, Y.-C.; Chen, Y.-H.; Matsumura, S.; Zou, J. Achieving $zT > 2$ in *p*-Type $AgSbTe_{2-x}Se_x$ Alloys via Exploring the Extra Light Valence Band and Introducing Dense Stacking Faults. *Adv. Energy Mater.* **2018**, *8*, 1702333.
(14) Zhang, G.; Kirk, B.; Jauregui, L. A.; Yang, H.; Xu, X.; Chen, Y. P.; Wu, Y. Rational Synthesis of Ultrathin *n*-type Bi_2Te_3 Nanowires with Enhanced Thermoelectric Properties. *Nano Lett.* **2012**, *12*, 56−60.
(15) Hong, M.; Chasapis, T. C.; Chen, Z.-G.; Yang, L.; Kanatzidis, M. G.; Snyder, G. J.; Zou, J. *n*-Type $Bi_2Te_{3-x}Se_x$ Nanoplates with Enhanced Thermoelectric Efficiency Driven by Wide-Frequency Phonon Scatterings and Synergistic Carrier Scatterings. *ACS Nano* **2016**, *10*, 4719−4727.
(16) Soni, A.; Zhao, Y. Y.; Yu, L. G.; Aik, M. K. K.; Dresselhaus, M. S.; Xiong, Q. H. Enhanced Thermoelectric Properties of Solution Grown $Bi_2Te_{3-x}Se_x$ Nanoplatelet Composites. *Nano Lett.* **2012**, *12*, 1203−1209.
(17) Wu, H.; Carrete, J.; Zhang, Z.; Qu, Y.; Shen, X.; Wang, Z.; Zhao, L.-D.; He, J. Strong Enhancement of Phonon Scattering through Nanoscale Grains in Lead Sulfide Thermoelectrics. *NPG Asia Mater.* **2014**, *6*, No. e108.
(18) Tan, G.; Shi, F.; Hao, S.; Chi, H.; Bailey, T. P.; Zhao, L.-D.; Uher, C.; Wolverton, C.; Dravid, V. P.; Kanatzidis, M. G. Valence Band Modification and High Thermoelectric Performance in SnTe Heavily Alloyed with MnTe. *J. Am. Chem. Soc.* **2015**, *137*, 11507−11516.
(19) Tan, G.; Shi, F.; Hao, S.; Zhao, L.-D.; Chi, H.; Zhang, X.; Uher, C.; Wolverton, C.; Dravid, V. P.; Kanatzidis, M. G. Non-Equilibrium Processing Leads to Record High Thermoelectric Figure of Merit in PbTe-SrTe. *Nat. Commun.* **2016**, *7*, 12167.
(20) Wu, H.; Chang, C.; Feng, D.; Xiao, Y.; Zhang, X.; Pei, Y.; Zheng, L.; Wu, D.; Gong, S.; Chen, Y.; He, J.; Kanatzidis, M. G.; Zhao, L.-D. Synergistically Optimized Electrical and Thermal Transport Properties of SnTe via Alloying High-Solubility MnTe. *Energy Environ. Sci.* **2015**, *8*, 3298−3312.
(21) Biswas, K.; He, J.; Blum, I. D.; Wu, C. I.; Hogan, T. P.; Seidman, D. N.; Dravid, V. P.; Kanatzidis, M. G. High-Performance Bulk Thermoelectrics with All-Scale Hierarchical Architectures. *Nature* **2012**, *489*, 414−418.
(22) He, J.; Blum, I. D.; Wang, H.-Q.; Girard, S. N.; Doak, J.; Zhao, L.-D.; Zheng, J.-C.; Casillas, G.; Wolverton, C.; Jose-Yacaman, M.; Seidman, D. N.; Kanatzidis, M. G.; Dravid, V. P. Morphology Control of Nanostructures: Na-Doped PbTe−PbS System. *Nano Lett.* **2012**, *12*, 5979−5984.
(23) Li, M.; Cortie, D. L.; Liu, J.; Yu, D.; Islam, S. M. K. N.; Zhao, L.; Mitchell, D. R. G.; Mole, R. A.; Cortie, M. B.; Dou, S.; Wang, X. Ultra-High Thermoelectric Performance in Graphene Incorporated Cu_2Se: Role of Mismatching Phonon Modes. *Nano Energy* **2018**, *53*, 993−1002.
(24) Nazrul Islam, S. M. K.; Li, M.; Aydemir, U.; Shi, X.; Chen, L.; Snyder, G. J.; Wang, X. Giant Enhancement of the Figure-of-Merit over a Broad Temperature Range in Nano-Boron Incorporated Cu_2Se. *J. Mater. Chem. A* **2018**, *6*, 18409−18416.
(25) Pei, Y.; Zheng, L.; Li, W.; Lin, S.; Chen, Z.; Wang, Y.; Xu, X.; Yu, H.; Chen, Y.; Ge, B. Interstitial Point Defect Scattering Contributing to High Thermoelectric Performance in SnTe. *Adv. Electron. Mater.* **2016**, *2*, 1600019.

DOI: 10.1021/jacs.8b12624
J. Am. Chem. Soc. 2019, 141, 1742−1748

(26) Hong, M.; Wang, Y.; Liu, W.; Matsumura, S.; Wang, H.; Zou, J.; Chen, Z.-G. Arrays of Planar Vacancies in Superior Thermoelectric $Ge_{1-x-y}Cd_xBi_yTe$ with Band Convergence. *Adv. Energy Mater.* **2018**, *8*, 1801837.
(27) Chen, Z.; Jian, Z.; Li, W.; Chang, Y.; Ge, B.; Hanus, R.; Yang, J.; Chen, Y.; Huang, M.; Snyder, G. J.; Pei, Y. Lattice Dislocations Enhancing Thermoelectric PbTe in Addition to Band Convergence. *Adv. Mater.* **2017**, *29*, 1606768.
(28) He, J. Q.; Girard, S. N.; Zheng, J. C.; Zhao, L. D.; Kanatzidis, M. G.; Dravid, V. P. Strong Phonon Scattering by Layer Structured PbSnS2 in PbTe Based Thermoelectric Materials. *Adv. Mater.* **2012**, *24*, 4440−4444.
(29) Liu, W.-S.; Zhang, B.-P.; Li, J.-F.; Zhao, L.-D. Thermoelectric Property of Fine-Grained $CoSb_3$ Skutterudite Compound Fabricated by Mechanical Alloying and Spark Plasma Sintering. *J. Phys. D: Appl. Phys.* **2007**, *40*, 566−572.
(30) Kim, W. Strategies for Engineering Phonon Transport in Thermoelectrics. *J. Mater. Chem. C* **2015**, *3*, 10336−10348.
(31) Pei, Y.; Wang, H.; Snyder, G. J. Band Engineering of Thermoelectric Materials. *Adv. Mater.* **2012**, *24*, 6125−35.
(32) Pei, Y.; Shi, X.; LaLonde, A.; Wang, H.; Chen, L.; Snyder, G. J. Convergence of Electronic Bands for High Performance Bulk Thermoelectrics. *Nature* **2011**, *473*, 66−69.
(33) Hong, M.; Chen, Z.-G.; Pei, Y.; Yang, L.; Zou, J. Limit of *zT* Enhancement in Rocksalt Structured Chalcogenides by Band Convergence. *Phys. Rev. B: Condens. Matter Mater. Phys.* **2016**, *94*, 161201.
(34) Moshwan, R.; Yang, L.; Zou, J.; Chen, Z.-G. Eco-Friendly SnTe Thermoelectric Materials: Progress and Future Challenges. *Adv. Funct. Mater.* **2017**, *27*, 1703278.
(35) Yang, L.; Chen, Z.-G.; Dargusch, M. S.; Zou, J. High Performance Thermoelectric Materials: Progress and Their Applications. *Adv. Energy Mater.* **2018**, *8*, 1701797.
(36) Perumal, S.; Roychowdhury, S.; Biswas, K. High Performance Thermoelectric Materials and Devices Based on GeTe. *J. Mater. Chem. C* **2016**, *4*, 7520−7536.
(37) Hong, M.; Chen, Z.-G.; Yang, L.; Zou, Y.-C.; Dargusch, M. S.; Wang, H.; Zou, J. Realizing *zT* of 2.3 in $Ge_{1-x-y}Sb_xIn_yTe$ via reducing the phase-transition temperature and introducing resonant energy doping. *Adv. Mater.* **2018**, *30*, 1705942.
(38) Li, J.; Zhang, X.; Lin, S.; Chen, Z.; Pei, Y. Realizing the High Thermoelectric Performance of GeTe by Sb-Doping and Se-Alloying. *Chem. Mater.* **2017**, *29*, 605−611.
(39) Li, J.; Chen, Z.; Zhang, X.; Sun, Y.; Yang, J.; Pei, Y. Electronic Origin of the High Thermoelectric Performance of GeTe among the *p*-type Group IV Monotellurides. *NPG Asia Mater.* **2017**, *9*, No. e353.
(40) Wu, D.; Zhao, L.; Hao, S.; Jiang, Q.; Zheng, F.; Doak, J. W.; Wu, H.; Chi, H.; Gelbstein, Y.; Uher, C.; Wolverton, C.; Kanatzidis, M.; He, J. Origin of the High Performance in GeTe-Based Thermoelectric Materials upon Bi_2Te_3 Doping. *J. Am. Chem. Soc.* **2014**, *136*, 11412−11419.
(41) Skelton, J. M.; Burton, L. A.; Parker, S. C.; Walsh, A.; Kim, C.-E.; Soon, A.; Buckeridge, J.; Sokol, A. A.; Catlow, C. R. A.; Togo, A.; Tanaka, I. Anharmonicity in the High-Temperature CMCM Phase of SnSe: Soft Modes and Three-Phonon Interactions. *Phys. Rev. Lett.* **2016**, *117*, 075502.
(42) Lindsay, L.; Broido, D. A.; Reinecke, T. L. First-Principles Determination of Ultrahigh Thermal Conductivity of Boron Arsenide: A Competitor for Diamond? *Phys. Rev. Lett.* **2013**, *111*, 025901.
(43) Togo, A.; Chaput, L.; Tanaka, I. Distributions of Phonon Lifetimes in Brillouin Zones. *Phys. Rev. B: Condens. Matter Mater. Phys.* **2015**, *91*, 094306.
(44) Lee, H. S.; Kim, B.-S.; Cho, C.-W.; Oh, M.-W.; Min, B.-K.; Park, S.-D.; Lee, H.-W. Herringbone Structure in GeTe-Based Thermoelectric Materials. *Acta Mater.* **2015**, *91*, 83−90.
(45) Wu, H.; Zhao, X.; Song, D.; Tian, F.; Wang, J.; Loh, K. P.; Pennycook, S. J. Progress and Prospects of Aberration-Corrected STEM for Functional Materials. *Ultramicroscopy* **2018**, *194*, 182−192.
(46) Pei, Y.; LaLonde, A. D.; Wang, H.; Snyder, G. J. Low Effective Mass Leading to High Thermoelectric Performance. *Energy Environ. Sci.* **2012**, *5*, 7963−7969.
(47) Wang, H.; LaLonde, A. D.; Pei, Y.; Snyder, G. J. The Criteria for Beneficial Disorder in Thermoelectric Solid Solutions. *Adv. Funct. Mater.* **2013**, *23*, 1586−1596.
(48) Wu, L.; Li, X.; Wang, S.; Zhang, T.; Yang, J.; Zhang, W.; Chen, L.; Yang, J. Resonant Level-Induced High Thermoelectric Response in Indium-Doped GeTe. *NPG Asia Mater.* **2017**, *9*, No. e343.
(49) Samanta, M.; Biswas, K. Low Thermal Conductivity and High Thermoelectric Performance in $(GeTe)_{1-2x}(GeSe)_x(GeS)_x$Competition between Solid Solution and Phase Separation. *J. Am. Chem. Soc.* **2017**, *139*, 9382−9391.
(50) Borup, K. A.; Toberer, E. S.; Zoltan, L. D.; Nakatsukasa, G.; Errico, M.; Fleurial, J.-P.; Iversen, B. B.; Snyder, G. J. Measurement of the Electrical Resistivity and Hall Coefficient at High Temperatures. *Rev. Sci. Instrum.* **2012**, *83*, 123902.
(51) Giannozzi, P.; Baroni, S.; Bonini, N.; Calandra, M.; Car, R.; Cavazzoni, C.; Ceresoli, D.; Chiarotti, G. L.; Cococcioni, M.; Dabo, I.; Corso, A. D.; Gironcoli, S. d.; Fabris, S.; Fratesi, G.; Gebauer, R.; Gerstmann, U.; Gougoussis, C.; Kokalj, A.; Lazzeri, M.; Martin-Samos, L.; Marzari, N.; Mauri, F.; Mazzarello, R.; Paolini, S.; Pasquarello, A.; Paulatto, L.; Sbraccia, C.; Scandolo, S.; Sclauzero, G.; Seitsonen, A. P.; Smogunov, A.; Umari, P.; Wentzcovitch, R. M. Quantum Espresso: A Modular and Open-Source Software Project for Quantum Simulations of Materials. *J. Phys.: Condens. Matter* **2009**, *21*, 395502.
(52) Perdew, J. P.; Burke, K.; Ernzerhof, M. Generalized Gradient Approximation Made Simple. *Phys. Rev. Lett.* **1996**, *77*, 3865−3868.
(53) Togo, A.; Tanaka, I. First Principles Phonon Calculations in Materials Science. *Scr. Mater.* **2015**, *108*, 1−5.
(54) Li, W.; Carrete, J.; Katcho, A.; Mingo, N. ShengBTE: a solver of the Boltzmann transport equation for phonons. *Comput. Phys. Commun.* **2014**, *185*, 1747−1758.

DOI: 10.1021/jacs.8b12624
J. Am. Chem. Soc. 2019, 141, 1742−1748

Supporting Information

Strong Phonon-Phonon Interactions Securing Extraordinary Thermoelectric $Ge_{1-x}Sb_xTe$ with Zn-Alloying Induced Band Alignment

Min Hong,[†,‡] Yuan Wang,[†] Tianli Feng[#,⊥] Qiang Sun,[‡] Shengduo Xu,[‡] Syo Matsumura,[§] Sokrates T. Pantelides,[#,⊥] Jin Zou,[*,†,‖] and Zhi-Gang Chen[*,†,‡]

[†] Centre for Future Materials, University of Southern Queensland, Springfield, Queensland 4300, Australia.

[‡] Materials Engineering, The University of Queensland, Brisbane, Queensland 4072, Australia.

[#] Department of Physics and Astronomy and Department of Electrical Engineering and Computer Science, Vanderbilt University, Nashville, Tennessee 37235, United States.

[⊥] Materials Science and Technology Division, Oak Ridge National Laboratory, Oak Ridge, Tennessee 37831, United States.

[§] Department of Applied Quantum Physics and Nuclear Engineering, Kyushu University, Motooka 744, Nishi-ku, Fukuoka 819-0395, Japan.

[‖] Centre for Microscopy and Microanalysis, The University of Queensland, Brisbane, Queensland 4072, Australia.

*Email: zhigang.chen@usq.edu.au, zhigang.chen@uq.edu.au, and j.zou@uq.edu.au

1. Modeling study of electronic transport

Thermoelectric properties of single band Kane model are given by[1]

Seebeck coefficient

$$S = \frac{k_B}{e}\left[\frac{F_{1,-2}^{1}(\eta,\beta)}{F_{1,-2}^{0}(\eta,\beta)} - \eta\right], \tag{S1}$$

Hall carrier concentration

$$n_H = \frac{N\left(2m_b^* k_B T\right)^{\frac{3}{2}}}{3\pi^2\hbar^3}\frac{F_{3/2,0}^{0}(\eta,\beta)}{A}, \tag{S2}$$

Hall carrier mobility

$$\mu_H = A\frac{2\pi\hbar^4 e C_l}{m_I^*\left(2m_b^* k_B T\right)^{3/2} E_{def}^2}\frac{3F_{1,-2}^{0}(\eta,\beta)}{F_{3/2,0}^{0}(\eta,\beta)}, \tag{S3}$$

Hall factor

$$A = \frac{3K(K+2)}{(2K+1)^2}\frac{F_{1/2,-4}^{0}F_{3/2,0}^{0}}{\left(F_{1,-2}^{0}\right)^2}, \tag{S4}$$

Electrical conductivity

$$\sigma = n_H\mu_H e = \frac{2e^2 N\hbar C_l}{\pi m_I^* E_{def}^2}F_{1,2}^{0}(\eta,\beta), \tag{S5}$$

Generalized Fermi integration

$$F_{m,k}^{n}(\eta,\beta) = \int_0^\infty\left[-\frac{\partial f(\eta)}{\partial\varepsilon}\right]\varepsilon^n\left(\varepsilon+\beta\varepsilon^2\right)^m\left[(1+2\beta\varepsilon)^2+2\right]^{\frac{k}{2}}d\varepsilon, \tag{S6}$$

Electrical thermal conductivity is calculated according to the Wiedemann–Franz law, namely

$$\kappa_e = L\sigma T, \tag{S7}$$

with L representing the Lorenz number, and given by

$$L = \left(\frac{k_B}{e}\right)^2\left[\frac{F_{1,-2}^{2}(\eta,\beta)}{F_{1,-2}^{0}(\eta,\beta)} - \left(\frac{F_{1,-2}^{1}(\eta,\beta)}{F_{1,-2}^{0}(\eta,\beta)}\right)^2\right]. \tag{S8}$$

In the above equations, η is the reduced Fermi level, $\beta = \frac{k_B T}{E_g}$ (E_g is the band gap) is the reciprocal reduced band gap, k_B is Boltzmann constant, e is the elementary charge, N is the band degeneracy, $\hbar$ is the reduced Planck constant, C_l is the combination of elastic constants, m_I^* is the inertial effective mass, and E_{def} is the deformation potential, respectively.[2,3]

2. Thermal stability examination of obtained maximal thermoelectric performance

The thermal stability of the obtained thermoelectric properties of $Ge_{0.86}Sb_{0.1}Zn_{0.04}Te$ was tested by three heating-cooling cycle measurements. Figure S1 shows the results. The obtained thermoelectric properties do not degenerate notably after three heating-cooling measurements.

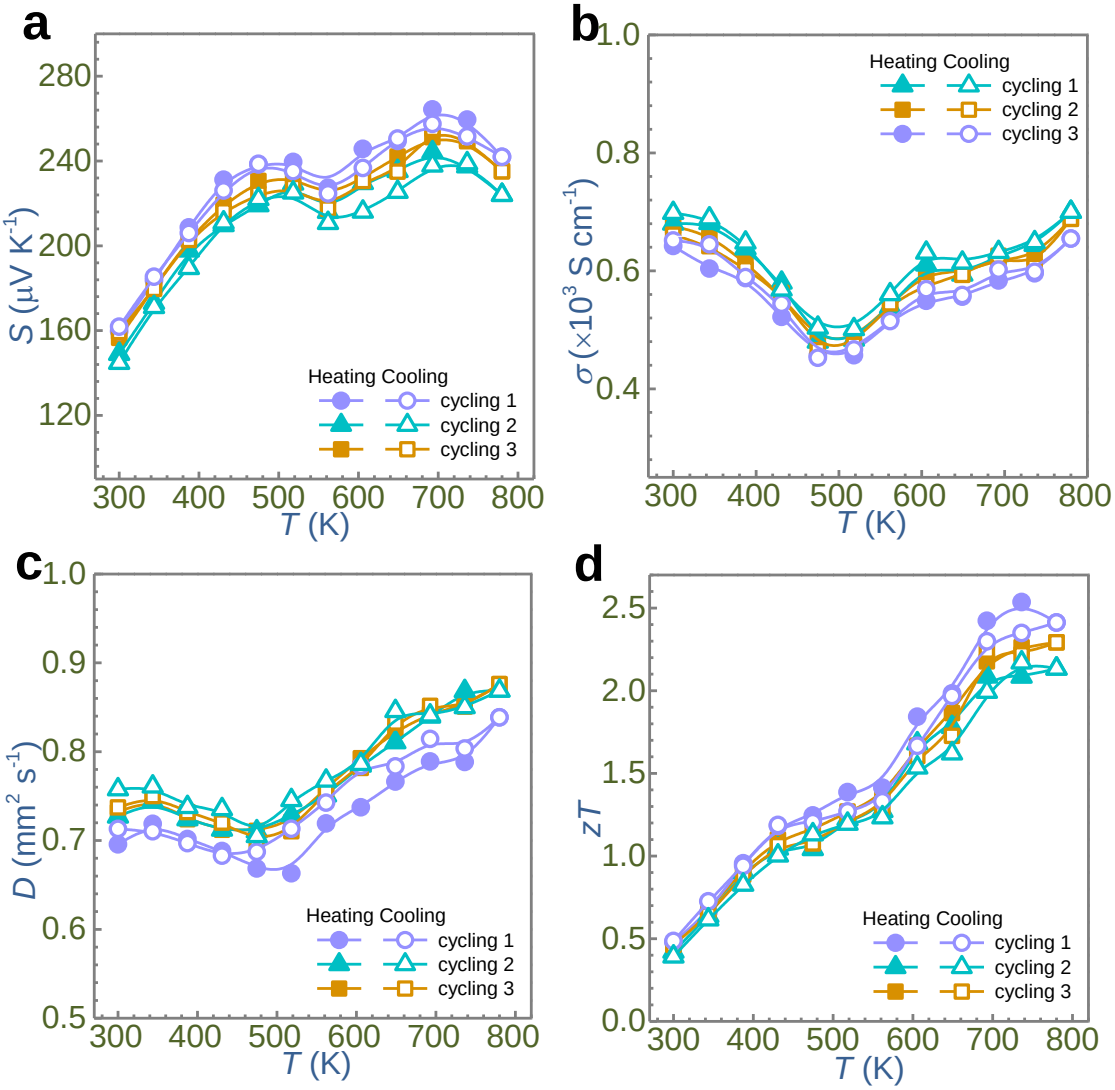

Figure S1 Temperature-dependent (a) *S*, (b) *σ*, (c) *D*, and (d) *zT* for $Ge_{0.86}Sb_{0.1}Zn_{0.04}Te$ measured through three heating-cooling cycles to test the thermal stability.

3. Phase examination of as-synthesized samples

Figure S2 and Figure S3 display the X-ray diffraction (XRD) patterns of as-synthesized $Ge_{1-x}Sb_xTe$ and $Ge_{0.9-y}Sb_{0.1}Zn_yTe$. XRD peaks in these samples can be indexed as the rhombohedral GeTe (*R*-GeTe). In Figure S2, the peak shifting towards low diffraction angle suggests the slight increase of lattice parameters due to the replacement of Sb with a large atomic radius on Ge sites.

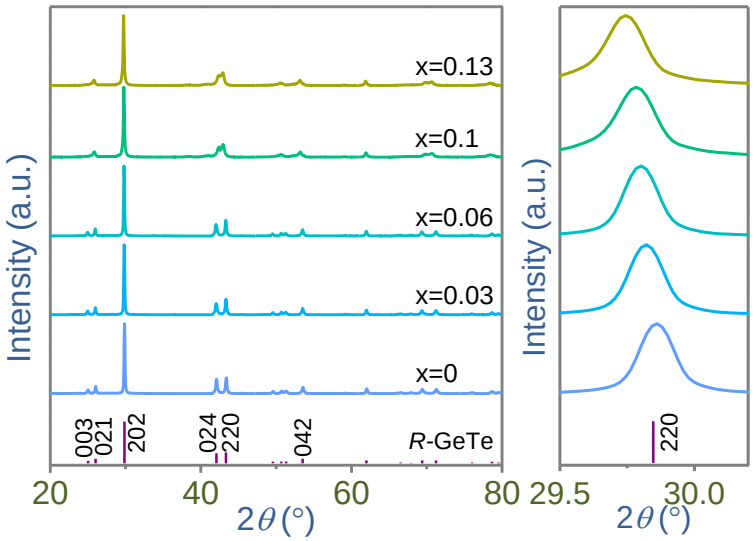

Figure S2 XRD patterns of $Ge_{1-x}Sb_xTe$ with the enlarged view showing the peak shifting.

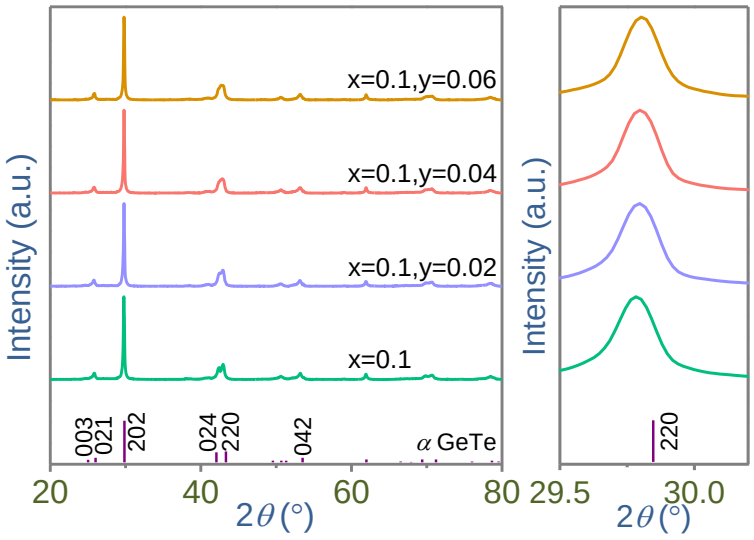

Figure S3 XRD patterns of $Ge_{0.9-y}Sb_{0.1}Zn_yTe$ with the enlarged view showing the peak shifting.

4. Measured thermoelectric properties and the determined L and κ_e

Figure S4 shows the measured thermoelectric properties as a function of temperature for sintered $Ge_{1-x-y}Sb_xZn_yTe$. The positive sign of S indicates the p-type semiconductor behavior with holes serving as the major free charge carriers.[4] As can be seen, upon increasing the alloying content and the additional Zn doping, S increases while σ decreases. The measured κ demonstrates a continuous decreasing trend with increasing Sb and Zn contents.

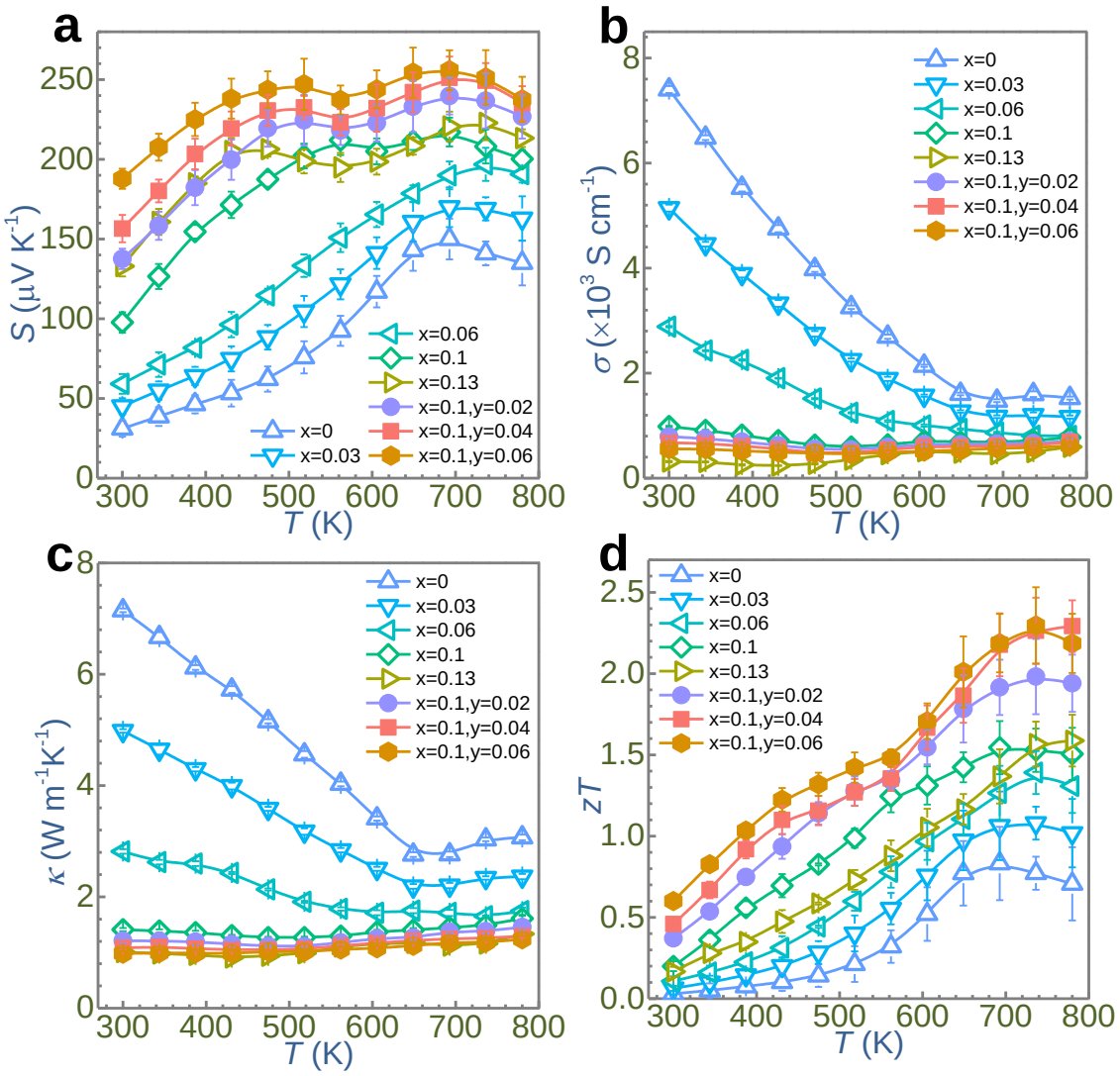

Figure S4 Measured temperature-dependent (a) S, (b) σ, (c) κ, and (d) zT for sintered $Ge_{1-x-y}Sb_xZn_yTe$ with different compositions.

With the determined Lorenz number (L) (Figure S5a), we calculate the electronic thermal conductivity (κ_e) according to the Wiedemann–Franz law.[5] Figure S5b shows the calculated κ_e, which decreases with increasing Sb and Zn content. The reduction in κ_e originates from the decreased σ. By subtracting κ_e from the total κ, we determine κ_l, as shown in Figure S5c.

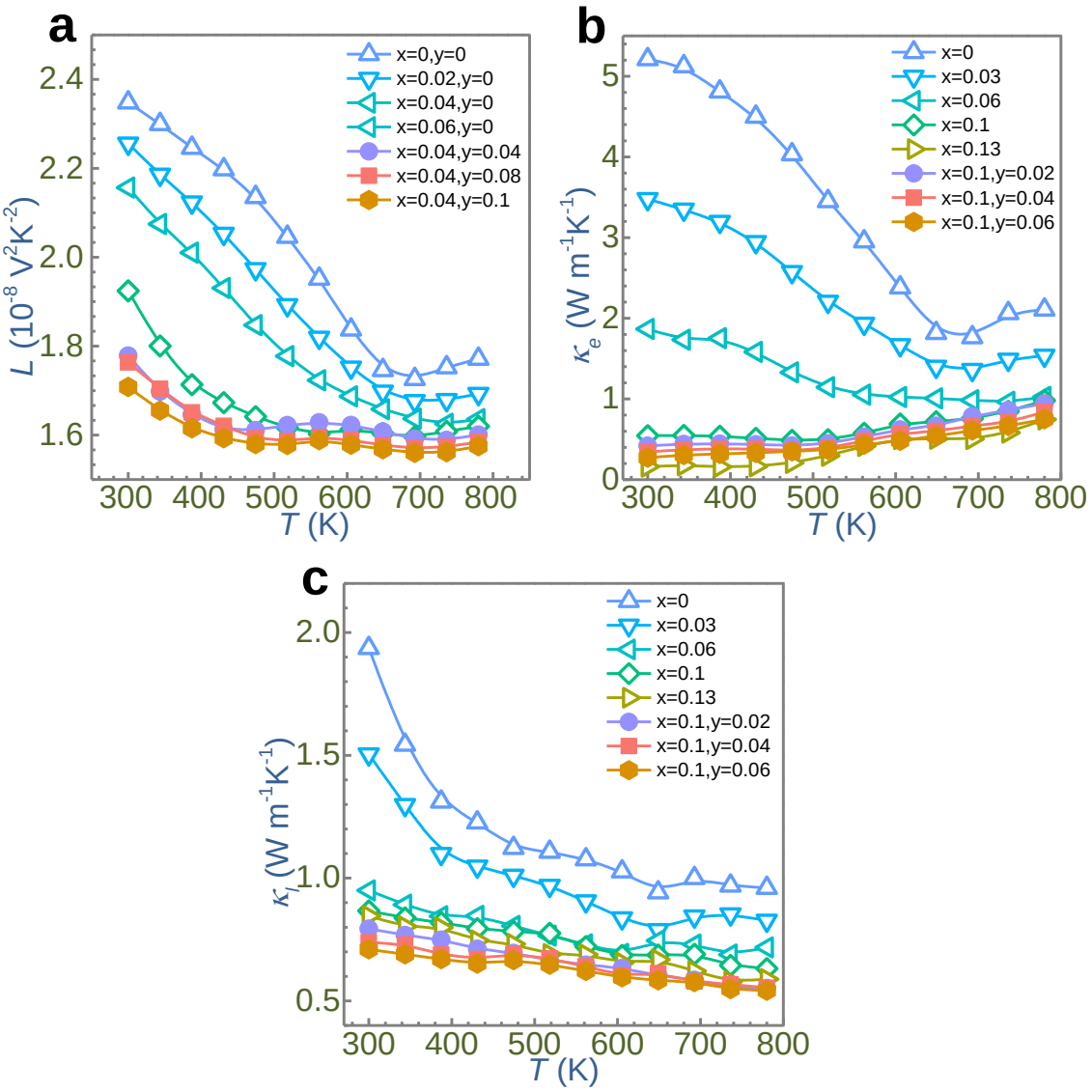

Figure S5 Calculated (a) L, (b) κ_e, and (c) κ_l for $Ge_{1-x-y}Sb_xZn_yTe$.

5. **Additional phonon dispersions and phonon-phonon scattering rates**

We calculated the phonon dispersions and phonon DOS for cubic structured GeTe and $Ge_{0.9}Sb_{0.1}Te$, shown in Figure S6. From Figure S6a, the phonon dispersion of cubic GeTe shows imaginary modes at Γ point, *i.e.*, the negative frequency of optical branches. The imaginary modes at Γ point indicate the instability of cubic GeTe at room temperature, which agrees with the absent of cubic GeTe at room temperature. The optical branches with negative frequency are much lower than the acoustic modes. Therefore, there is no frequency gap in cubic GeTe. In the phonon dispersion of $Ge_{0.9}Sb_{0.1}Te$ (Figure S6c), we can still observe the imaginary modes at Γ point. The imaginary modes of cubic GeTe are due to the instability. We cannot deduce the strength of acoustic-optical phonon scattering according to the frequency gap in cubic GeTe.

We calculated the phonon dispersion and phonon density-of-states for rhombohedral structured GeTe based on the 2x2x2 supercell. Figure S7a and b show the calculated phonon dispersion and phonon density-of-states, from which we can observe the frequency gap (marked by red dash lines) near 3 THz. This observation agrees with the observed frequency gap near 3 THz in the phonon dispersion of GeTe calculated based on the primitive cell.

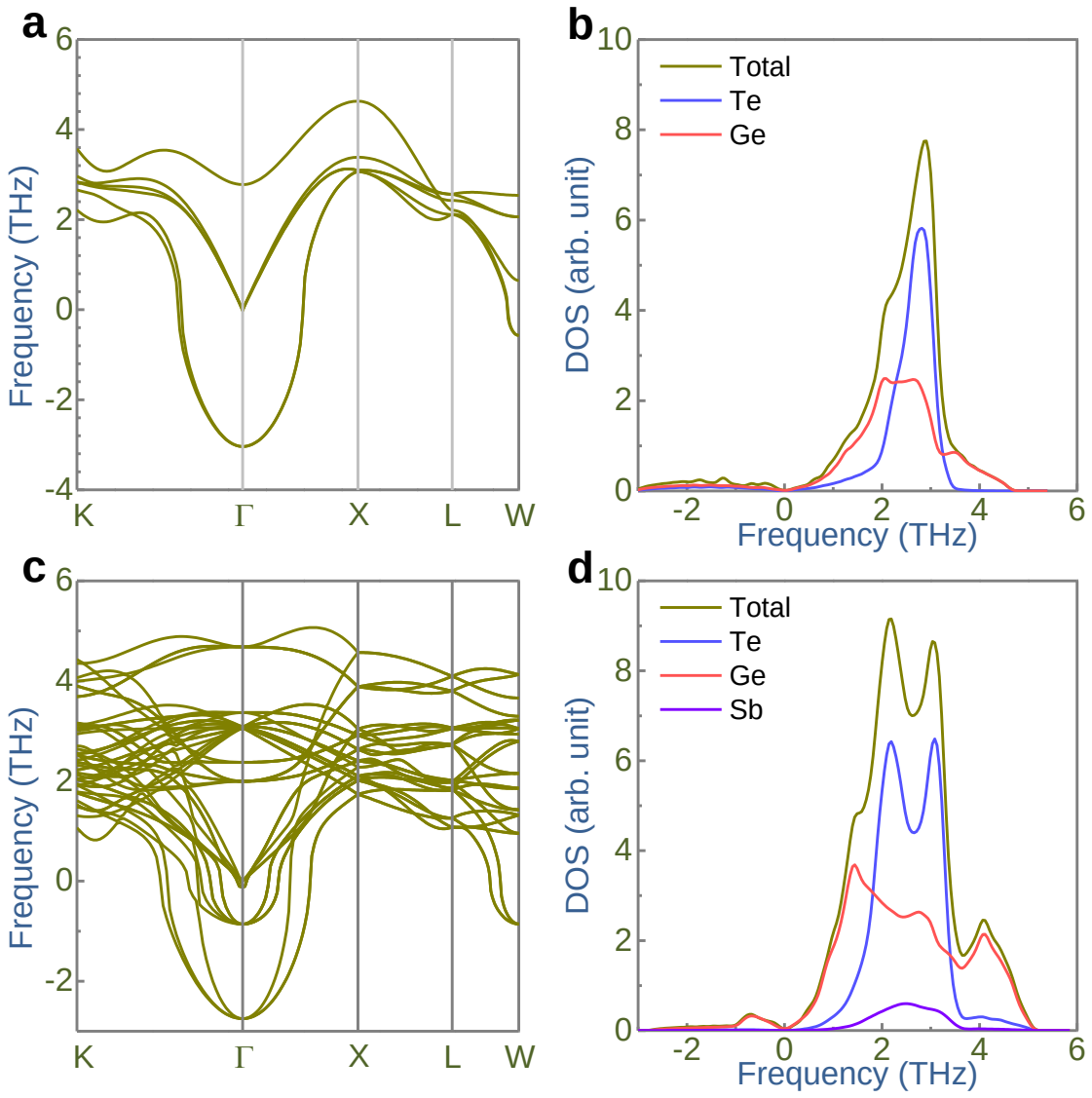

Figure S6 Calculated phonon dispersions for cubic structured (a) GeTe and (c) $Ge_{1-x}Sb_xTe$. Calculated phonon density-of-states (DOS) for cubic structured (b) GeTe and (d) $Ge_{1-x}Sb_xTe$.

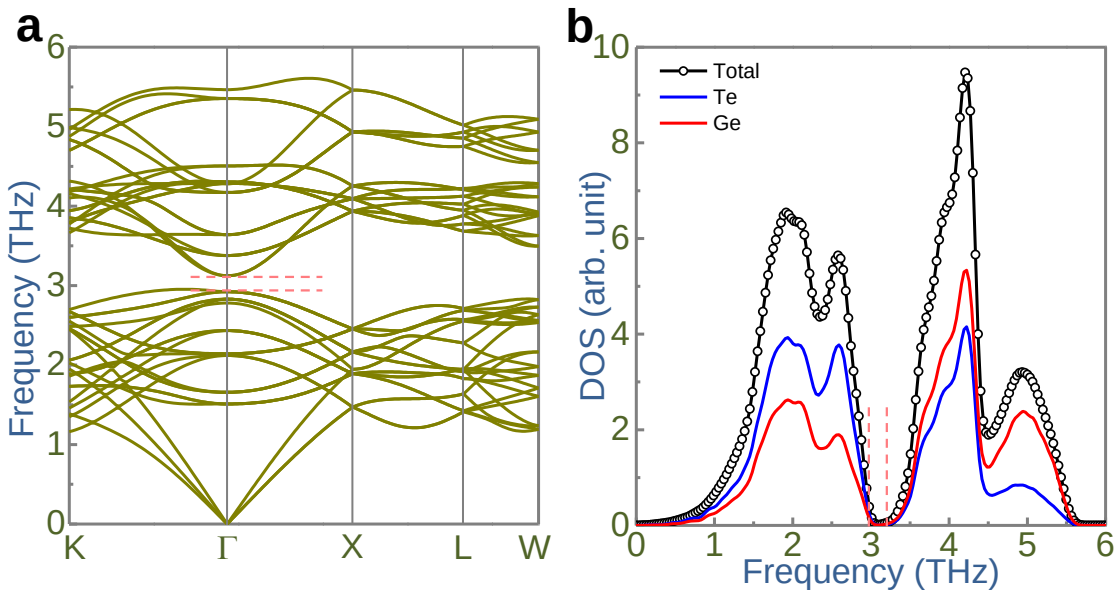

Figure S7 We calculated the phonon dispersion and phonon density-of-states for GeTe based on the 2x2x2 supercell. Figure R3a and b show the calculated phonon dispersion and phonon density-of-states, from which we can observe the frequency gap (marked by red dash lines) near 3 THz. This observation agrees with the observed frequency gap near 3 THz in the phonon dispersion of GeTe calculated based on the primitive cell.

To provide direct evidence of enhanced phonon-phonon interactions, we calculated the phonon scattering rate, shown in Figure S8. As can be seen, Sb alloying with a ratio of 10 % increases the scattering rate.

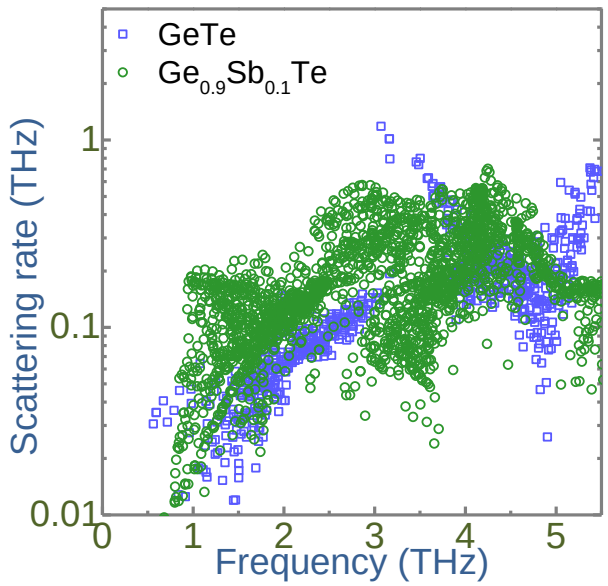

Figure S8 Calculated scattering rate of phonon-phonon interactions over the studied phonon frequency range.

6. Additional TEM images to characterize the microstructures

Figure S9 is the high-angle annular dark-field (HAADF) scanning TEM image taken from $Ge_{0.86}Sb_{0.1}Zn_{0.04}Te$. We can observe the nanoprecipitates with dark contrast, indicating that the component element of nanoprecipitates is lighter than the matrix.

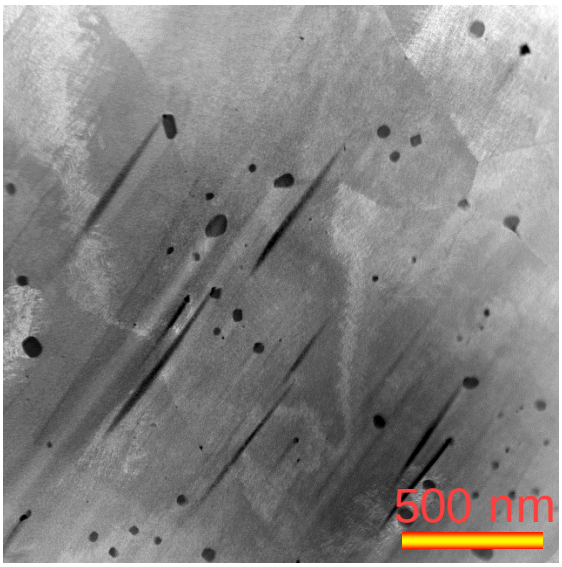

Figure S9 High-angle annular dark-field (HAADF) scanning TEM image taken from $Ge_{0.86}Sb_{0.1}Zn_{0.04}Te$.

7. Measured Hall data as a function of temperature

Figure S10a exhibits the measured Hall coefficients (R_H) for $Ge_{1-x-y}Sb_xZn_yTe$ over the studied temperature range. Then Figure S10b and c show the measured Hall carrier concentration (n_H) and Hall carrier mobility (μ_H) of as-synthesized samples.

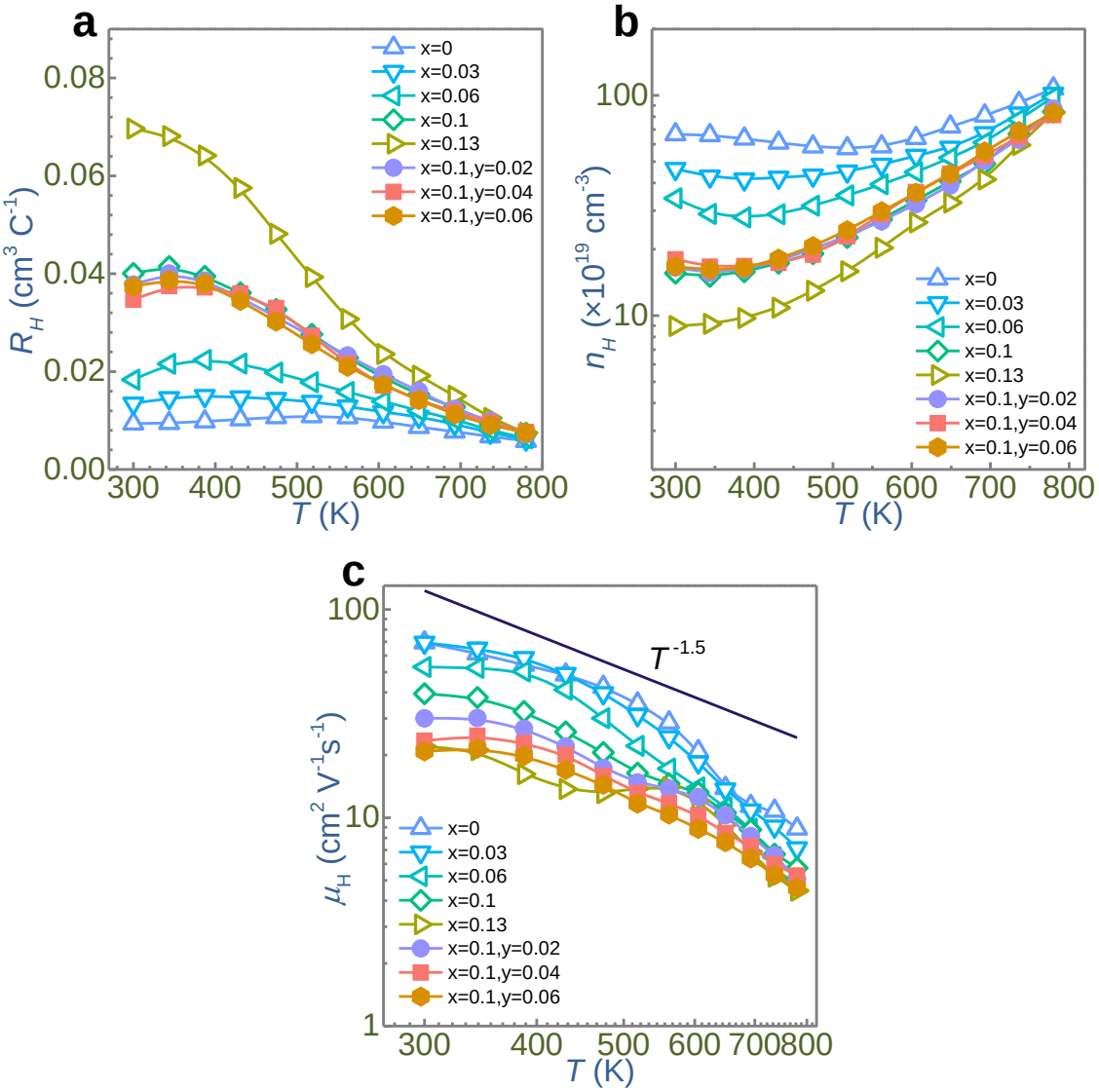

Figure S10 (a) R_H, (b) n_H, and (c) μ_H as a function of temperature for $Ge_{1-x-y}Sb_xZn_yTe$.

8. Chemical nature of band structures for GeTe

To examine the orbital characters of band structures for both rhombohedral and cubic GeTe, we calculated the band structures and incorporated the orbital characters, as shown in Figure S11a and b. The orbital weights are proportional to the symbol size. Two valence band edges with a ΔE at Σ and L points are observed in the band structure of GeTe. In rhombohedral GeTe, the primary valence band is at Σ and secondary valence band is at L. In cubic GeTe, the primary valence band is at L and secondary valence band is at Σ points. While Ge_$4p^2$ and Te_$5p^4$ dominate the conduction band and valence band near the gap region, respectively, Ge_$4s^2$ and Te_$5s^2$ are the main contributions to the two low-lying valence bands, which agrees with the calculated DOS and PDOS, as shown in Figure S11c and d. Weak spots of Ge_$4s^2$ are found in the valence band edges in both rhombohedral and cubic GeTe. Furthermore, in Figure S11e and f, the orbital weights for the occupied molecular orbital (HOMO) are projected along the studied high-symmetry points for rhombohedral and cubic GeTe, respectively. As can be seen, it is clear to observe the Ge_$4s^2$ orbitals in the HOMO. Figure S12 shows the band structure configuration of ZnTe. As can be seen, the valence band edge and conduction band are dominated by Te_$5p^4$ and Zn_$4s^2$, respectively. The lone pair of s^2 does not exist in Zn, which is commonly bonded with Te in the tetrahedral coordination. The comparison of band structure configurations of GeTe and ZnTe suggests that the orbital character of Ge_$4s^2$ lone pair electrons leads to the energy offset between the multiple valence band edges. Therefore, doping Zn atoms on Zn sites can decrease the energy offset by partially reducing the Ge_$4s^2$ character of HOMO of GeTe.

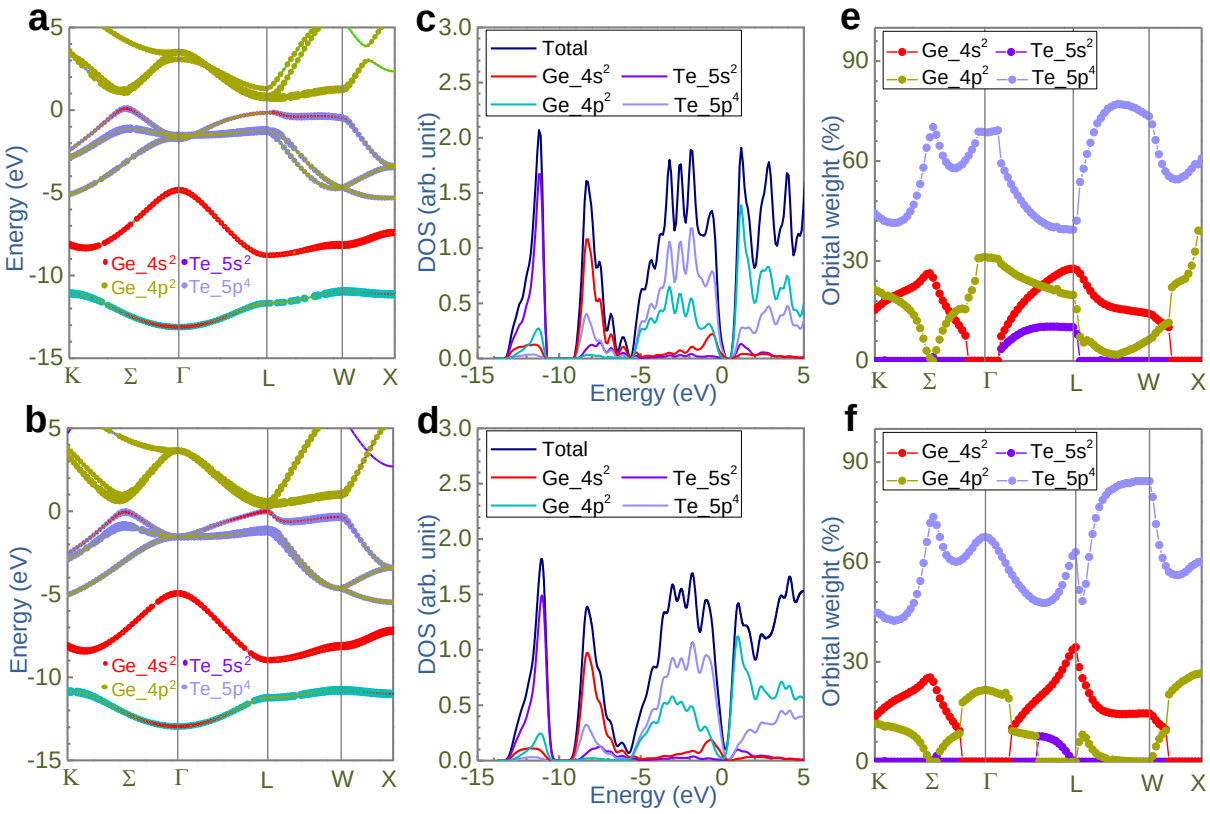

Figure S11 Band structures including SOC of rhombohedral (a) and cubic (b) GeTe. DOS and projected DOS of Ge_4s^2, Ge_4p^2, Te_5s^2, and Te_5p^4 of rhombohedral (c) and cubic (d) GeTe. The presented orbital weights of Ge_4s^2, Ge_4p^2, Te_5s^2, and Te_5p^4 are proportional to the corresponding symbol size. Orbital weights for HOMO projected along the high symmetric points of rhombohedral (e) and cubic (f) GeTe.

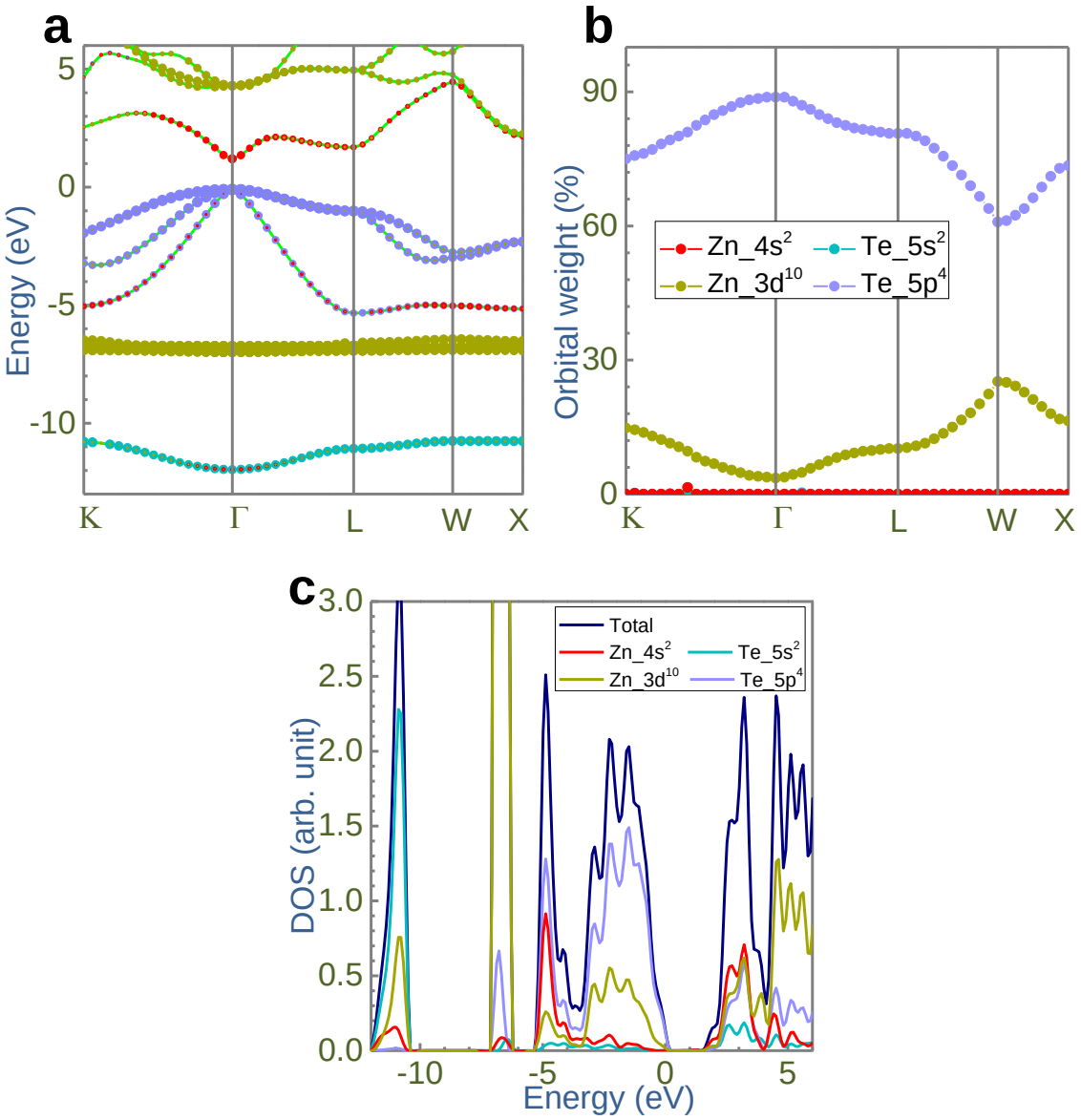

Figure S12 (a) Band structures of ZnTe. The presented orbital weights of Zn_4s^2, Zn_3d^{10}, Te_5s^2, and Te_5p^4 are proportional to the corresponding symbol size. (b) DOS and PDOS of ZnTe. (c) Orbital weights of Zn and Te for the highest valence band projected along the high-symmetry points.

9. Calculated DOS and PDOS for $Ge_{1-x-y}Sb_xZn_yTe$

Figure S13 shows the calculated density of states (DOS) and the projected DOS (PDOS) for rhombohedral and cubic $Ge_{1-x-y}Sb_xZn_yTe$. As can be seen, PDOS of Zn_4s^2 locates near the conduction band. Therefore, we can observe the impurity band induced by Zn doping in both rhombohedral and cubic $Ge_{1-x}Sb_xTe$.

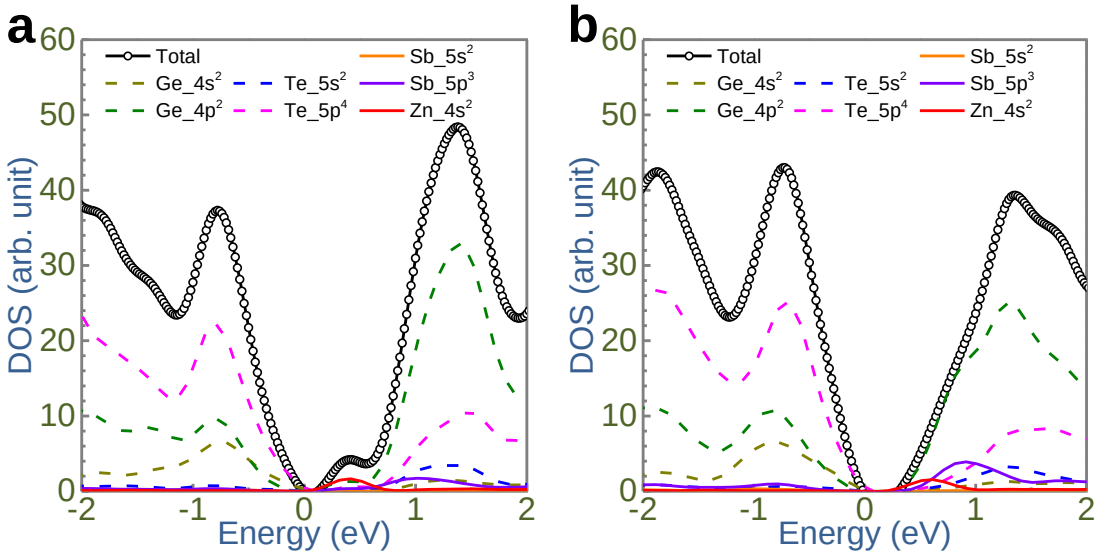

Figure S13 DOS and projected DOS of rhombohedral (a) and cubic (b) $Ge_{1-x-y}Sb_xZn_yTe$.

10. Measured thermal diffusivity, density of sintered pellets, and specific heat

Figure S14 shows the measured thermal diffusivity (D). As can be seen, alloying with Sb can considerably decrease D.

Figure S15 shows the measured the specific heat (C_p) for $Ge_{0.86}Sb_{0.1}Zn_{0.04}Te$ under heating rates of 10 K min^{-1} and 5 K min^{-1}, compared with the C_p estimated by Delong Petit law. As can be seen, the measured Cp varies under different heating rates, and the Cp estimated by Delong Petit approaches the average value of measured results.

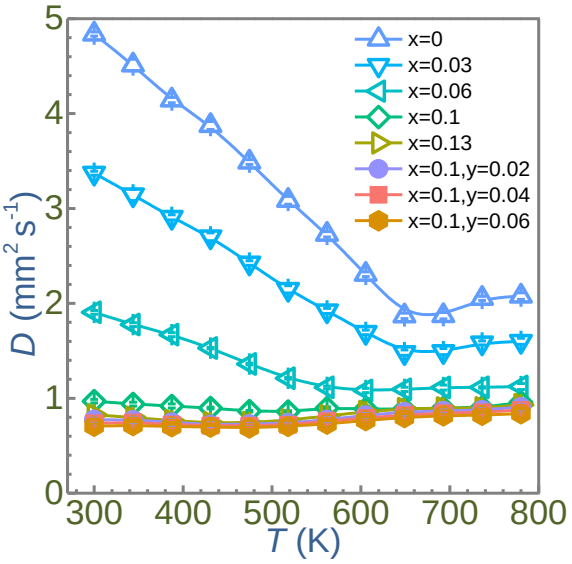

Figure S14 Measured thermal diffusivity (D) as a function of temperature for $Ge_{1-x-y}Sb_xZn_yTe$.

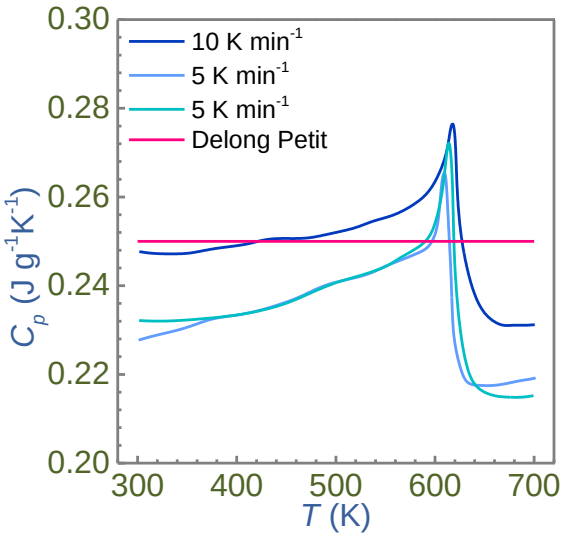

Figure S15 Specific heat (C_p) for $Ge_{0.86}Sb_{0.1}Zn_{0.04}Te$ measured under different heating rates compared with the C_p estimated by Delong Petit law.

Table S1 Density of sintered samples determined by Archimedes' method.

$Ge_{1-x}Sb_xTe$	Density (g cm^{-3})	Relative density (%)
x=0	6.01	97.88
x=0.03	6.06	98.70
x=0.06	5.92	96.42
x=0.1	5.99	97.56
x=0.13	5.86	95.44
$Ge_{0.9-y}Sb_{0.1}Zn_yTe$	Density (g cm^{-3})	Relative density (%)
y=0.02	5.96	97.07
y=0.04	6.06	98.70
y=0.06	5.98	97.39

References

(1) Hong, M.; Chen, Z.-G.; Pei, Y.; Yang, L.; Zou, J. Limit of *zT* Enhancement in Rocksalt Structured Chalcogenides by Band Convergence. *Phys. Rev. B* **2016,** *94*, 161201.

(2) Pei, Y.; Gibbs, Z. M.; Balke, B.; Zeier, W. G.; Snyder, G. J. Optimum Carrier Concentration in *n*-type PbTe Thermoelectrics. *Adv. Energy Mater.* **2014,** *4*, 1400486.

(3) Liu, W.; Lukas, K. C.; McEnaney, K.; Lee, S.; Zhang, Q.; Opeil, C. P.; Chen, G.; Ren, Z. Studies on the Bi_2Te_3-Bi_2Se_3-Bi_2S_3 System for Mid-Temperature Thermoelectric Energy Conversion. *Energy Environ. Sci.* **2013,** *6*, 552-560.

(4) Pei, Y.; LaLonde, A. D.; Wang, H.; Snyder, G. J. Low Effective Mass Leading to High Thermoelectric Performance. *Energy Environ. Sci.* **2012,** *5*, 7963-7969.

(5) Hong, M.; Chen, Z.-G.; Zou, J. Fundamental and Progress of Bi_2Te_3 -Based Thermoelectric Materials. *Chin. Phys. B* **2018,** *27*, 048403.